Advanced Sensor Research

ADVANCED SENSOR RESEARCH Open Access

www.advsensorres.com

RESEARCH ARTICLE OPEN ACCESS

CO_2 Detection Using Potentiometric Sensors Based on PIM-1/DES Membranes

Eugenio De Nardo[1,2] | Simone Martellone[1,2] | Valentina Bugliarelli[1,2] | Davide Molino[1,2] | Giuseppe Ferraro[1] | Stefania Lettieri[1] | Pietro Zaccagnini[1,2] | Marco Etzi[2] | Erik Piatti[1] | Mattia Bartoli[2,3] | Andrea Lamberti[1,2] | Candido Fabrizio Pirri[1,2] | Angelica Monica Chiodoni[1] | Sergio Bocchini[1,2,3]

[1]Department of Applied Science and Technology, Politecnico di Torino, Turin, Italy | [2]Center For Sustainable Future Technologies (CSFT), Istituto Italiano di Tecnologia (IIT), Turin, Italy | [3]Consorzio Interuniversitario Nazionale per la Scienza e Tecnologia dei Materiali (INSTM), Florence, Italy

Correspondence: Mattia Bartoli (mattia.bartoli@iit.it) | Sergio Bocchini (sergio.bocchini@polito.it)

Received: 12 December 2025 | **Revised:** 25 June 2026 | **Accepted:** 8 July 2026

Keywords: deep eutectic solvent | gas sensing | polymer of intrinsic microporosity

ABSTRACT

Polymers of Intrinsic Microporosity (PIMs) are a class of polymers characterized by a native microporous network resulting in a high surface area. PIMs also display a highly tunable and efficient gas permeability, attracting a lot of attention in several electrochemical applications. In this work. PIM-1 was combined with a deep eutectic solvent (DES) for the production of a potentiometric sensor for CO_2. This study reports the synthesis of both components, the fabrication of composite membranes via solvent casting and impregnation, and their evaluation as CO_2 responsive materials together with a comprehensive characterization. The PIM-1/DES materials demonstrated efficient CO_2 capture and release behavior with open-circuit voltage responses recorded under controlled CO_2 exposure and adsorption–desorption cycling with full recovery. The membrane exhibited a response of 29 s in pure CO_2 with a recovery time of 240 s. The sensors followed a logarithmic correlation between CO_2 concentration and voltage variation and it showed a sensitivity of up to 9.6 mV/%CO_2. These findings indicate that the developed sensor offers high reproducibility, fast response, and reliable detection of variable CO_2 levels, underscoring its strong potential for practical implementation in environmental and industrial monitoring applications.

1 | Introduction

During the last decades, Deep Eutectic Solvents (DESs) have gained significant attention due to their unique physicochemical properties suitable for a wide range of applications including electrochemical sensor technology [1–3]. DESs are composed of two strongly interacting components forming a eutectic mixture [4, 5], and their synthesis are generally recognized as based on green and simple methodology that typically employs non-toxic components without generating secondary products [6, 7]. While the individual components are solid below 100°C, their mixture remains liquid. Since their introduction by Abbott et al. [8] in 2001, DES have emerged as promising and versatile alternatives to ionic liquids (IL), finding applications across various fields especially the electrochemical one [9].

Fuchs et al. [10]. highlighted the electrochemical behavior of graphene in choline chloride/ethylene glycol-based DES (12CE) demonstrating good stability and high value of electron transfer in 12CE. Gavello et al. [11] showed how a choline chloride/glycerol DES displayed superior performance with respect to ILs for hydrogen loading in a metallic electrode. Arab et al. [12]. developed a high-sensitivity electrochemical sensor for the detection of paracetamol and 4-aminophenol utilizing a multiwalled carbon nanotubes/DES modified glassy carbon electrode highlighting the role of DES in enhancing sensor performance. An interesting

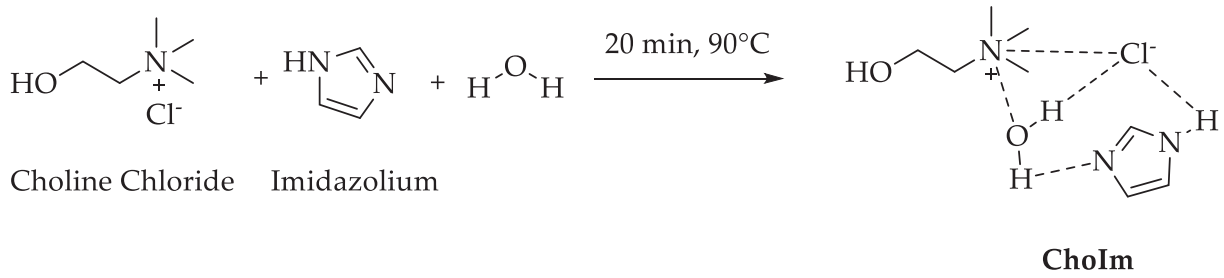

FIGURE 1 | Reaction pathways of ChoIm synthesis.

advancement in the production of sensors beyond traditional electrode materials [13–20] is the utilization of polymer-based and nanomaterials active species [13–28]. Shahrbabaki et al. [29]. developed an amine-functionalized copolymer able to act as chemiresistive, low-cost, flexible, and reversible CO_2 sensor with a response time of 6 min and a detection range of 1-0.01% of residual pressure.

Polymer membrane based CO_2 sensors can exploit a high and selective gas transport together with mechanical flexibility and merging with flexible and wearable platforms speeding their use as resistive electrochemical sensors CO_2. The great functionalizability of polymeric membranes has allowed to tailor the adsorption and transport CO_2 through acid–base interactions or fixed carrier sites improving the selectivity toward N_2, O_2 reducing the cross-sensitivity [30]. Furthermore, polymer membrane sensors can operate at room temperature contrary to plenty of metal-oxide resistive sensors [31]. Additionally, metal oxide based resistive sensors for CO_2 detection can show baseline drift and great susceptibility to humidity and other gaseous interferents limiting long-term stability and increase maintenance burdens even if their performances are greater in for response time. Alternatively, optical CO_2 sensors can be used to achieves high accuracy and stability but their assembling is far too complex than electrochemical sensors and they can not be easily integrated in flexible systems or miniaturized [32–35].

Accordingly, great effort has been dedicated to improve the polymer based sensors toward the current state of the art. Mohamed et al. [36]. reported an interesting approach based on the use of polyhedral silsesquioxane oligomeric microporous systems able to promote at the same time the CO_2 uptake and metal sensing. As discussed by Topuz et al. [37]., polymers of intrinsic microporosity (PIMs) represent a solid alternative and a new promising approach for CO_2 sensing through electrochemical methods due to their unique properties of gas adsorption, permeability and chemical features [38–40]. Goodwin et al. [41]. produced a PIM based material containing graphene flakes with the ability of sensing plenty of gases including NO_2, NH_3, NO, CH_4 and CO_2 in the range from 1 to up to 50 ppm. Zhou et al. [42]. prepared a resistive PIM-1 sensor with a fast response up to 60 s at room temperature with a resistance increase of high resistance up to 10^7 after 5 min.

In this work, a PIM-1 containing DES (PIM-1_ChoIm) was produced using Choline chloride and imidazolium (ChoIm) and was used as a potentiometric electrochemical sensor for CO_2 detection. PIM-1_ChoIm was deeply investigated in order to evaluate comprehensively both physicochemical and morphological properties to establish a solid base for the enhancement in sensing properties.

2 | Materials and Methods

2.1 | Materials

All solvents and reagents were used as received without further purification. 2,3,5,6-Tetrafluoroterephtalonitrile was purchased from FluoroChem (Hadfield, UK). Choline chloride (≥ 98%) and imidazolium (purity ≥ 99%) and all the other reagents and solvents were purchased from Merck-Sigma–Aldrich (St. Louis, MO, USA).

2.2 | Methods

2.2.1 | Synthesis of PIM-1

PIM-1 was synthesized following a previously reported procedure [43]. Briefly, a mixture of anhydrous K_2CO_3 (5.53 g, 0.04 mol, FW = 138.205), 3,3,3′,3′-Tetramethyl-1,1′-spirobiindane-5,5′,6,6′-tetraol (3 g, 0.008813 mol, FW = 340.41) and 2,3,5,6-Tetrafluoroterephthalonitrile (1.76 g, 0.008813 mol, FW = 200.096) in dry DMF (60 mL) was stirred at 65°C for 72 h under N_2 atmosphere. The crude was then poured in 400 mL of DI water, and the precipitate was washed by centrifugation several times in water and methanol. After drying under vacuum overnight, a bright yellow solid was obtained in a quantitative yield [44].

2.2.2 | Synthesis of ChoIm

Choline chloride and imidazolium were combined in a molar ratio of 3:7 with 2% w/w water. The mixture was heated to 90°C and stirred for 20 min [45] (Figure 1). ChoIm was outgassed under vacuum at 80°C overnight until constant [46] (Figure 1).

2.2.3 | PIM-1_ ChoIm Based Membrane Preparation

A bare PIM-1 membrane was prepared using a solvent-casting method. PIM-1 was dissolved in $CHCl_3$ to a total concentration of 5 wt.% and stirred at 40°C for 15 min. The solution was then cast onto a leveled aluminum substrate at room temperature. The resultant membrane was dried under vacuum at 40°C for at

TABLE 1 | Membrane measured thicknesses and corresponding densities.

Membrane	Thickness (μm)	Density (g cm^{-3})
PIM-1	14.9 ± 1.5	1.06 ± 0.01
PIM-1_ ChoIm	18.6 ± 10.0	1.35 ± 0.01

least 16 h to ensure the removal of any remaining solvent traces. To impregnate the membrane, the dried PIM-1 membrane was wetted with ChoIm. The membrane underwent three cycles of vacuum and ambient pressure to facilitate thorough impregnation. Following this, the membrane was stored in ChoIm under vacuum at room temperature for 1 h. Finally, the membrane was transferred onto filter paper to remove any excess ChoIm and named PIM-1_ChoIm as reported by Molino et al. [21].

2.2.4 | PIM-1_ ChoIm Based Membrane

To calculate the density of the membranes, predefined areas were cut, weighed, and their volumes were calculated based on the measured thickness. Membrane thicknesses were measured using a micrometer thickness gauge, averaging the measurements from five randomly selected points on each membrane (Table 1). The measured thicknesses of the membranes are lower than 20 μm. The densities of the membranes were found to be between 0.558 and 1.272 g/cm^3.

2.3 | Characterization of ChoIm and PIM-1_ ChoIm Based Membrane

Conductivity measurements were carried out using a standard glass conductivity cell from AMEL, with two symmetric platinum electrodes (cell constant provided by the producer K = 1). Performing an impedance spectroscopy measurement on the sample and evaluating the value of the Re(Z) when Im(Z) = 0 Ω, it is possible to determine the conductivity, which in this case is 25,27 mS cm^{-1}.

To determine the electrochemical stability window (ESW), a standard T-cell from Swagelok exploiting 12 mm diameter electrodes was used. The separator was the glass fiber of grade D (GF/D) from Whatman, rinsed with 400 μL of electrolyte, the working electrode was platinum disk, while counter electrode and reference were both activated carbons. The choice is motivated by the good stability of the materials with Cl^- ions and water presence. Linear sweep voltammetry at 5 mV s^{-1} was used to determine anodic and cathodic stability limit. Fresh DES was used for each measurement.

Furtheremore, a device with 2 commercial gas diffusion electrodes (Sigracet 22 BB), divided by Whatmann glass fiber grade C, soaked with 200 μL of DES was assembled, and the cell was subjected to cyclic voltammetry, gradually increasing the maximum applied voltage from 0.5 V up to 1 V. In details the tested voltage ranges were: 0–0.5 V, -0.5–0.5 V, 0–0.7 V, -0.7–0.7 V, 0–1 V, -1–1 V. The measurements were carried out using a PAT-cell setup from EL-cell Gmbh.

Attenuated total reflection infrared spectroscopy (ATR-IR) was employed to analyze the membranes. The measurements were performed with a Bruker Tensor II Fourier transform spectrometer. Spectra were obtained by averaging 64 scans (including 64 background scans) within the 4000–600 cm^{-1} range at a resolution of 2 cm^{-1}.

Thermogravimetric analysis coupled with infrared absorption (TGA-IR) was conducted using a NETZSCH TG 209 F1 thermogravimetric analyzer connected to a Bruker TENSOR II infrared spectrometer via a transfer line maintained at 230°C. The IR gas cell of the spectrometer was heated to 200°C. Approximately 3 mg of samples were placed in alumina pans and heated from 30°C to 800°C at a rate of 20 K/min under a nitrogen flow of 40 mL/min. The FTIR spectra were recorded in absorbance mode over the range of 4400–600 cm^{-1}. The first derivative of the weight profile (DTG) was computed using Netzsch Proteus Analysis software to enhance the resolution of the primary thermal decomposition stages.

DSC was carried out by means of a Netzsch DSC 204 F1 Phoenix in the temperature range from −70°C to 110°C at a heating/cooling rate of 20°C min^{-1} under N_2 flux. A heat–cool– heat procedure was performed, and the glass transition temperature (T_g) was taken at the inflection point of the glass transition step in the third heating cycle. The data obtained were processed with Netzsch Proteus Analysis software.

Field emission scanning electron microscopy (FESEM) was carried out using a Zeiss Supra 25 (Oberkochen, Germany). Membrane thickness was determined using a Digimatic Indicator (IDC-112B-5) with a precision of 1 μm. Thickness values were reported as averages derived from at least 25 measurements taken at different points across the membrane.

Atomic force microscopy measurements were carried out in ambient conditions using a Bruker Innova microscope in tapping mode, with commercial silicon tips having a nominal resonance frequency of 300 kHz (TAP300Al-G). Image analysis and post-processing were performed using Gwyddion software [47].

Viscosity measurement was conducted with Anton Paar MCR 702e rheometer quipped with a parallel-plate geometry, with the temperature maintained at 25°C. The sample was loaded between the plates with a gap of 0.30 mm. It was then allowed to equilibrate under quiescent conditions (shear rate = 0 s^{-1}) to eliminate any shear history. pH measurement was carried out with a bench XS pH 8 PRO

2.4 | CO_2 Absorption Tests

CO_2 absorption measurements were performed by first subjecting the sample to a nitrogen flow of 20 mL/min at 40°C for 1 min to remove any pre-absorbed gases. The sample was then cooled to 25°C and maintained under a nitrogen flow for 120 min to stabilize the initial mass, recorded at minute 180. At 25°C, the gas flow was switched to a mixture of N_2 and CO_2 (12 mL/min of N_2 and 8 mL/min of CO_2) for a duration of 10 h to monitor the absorption process, with the final mass measured at minute 780. Subsequently, the gas flow was reverted to pure nitrogen, allowing

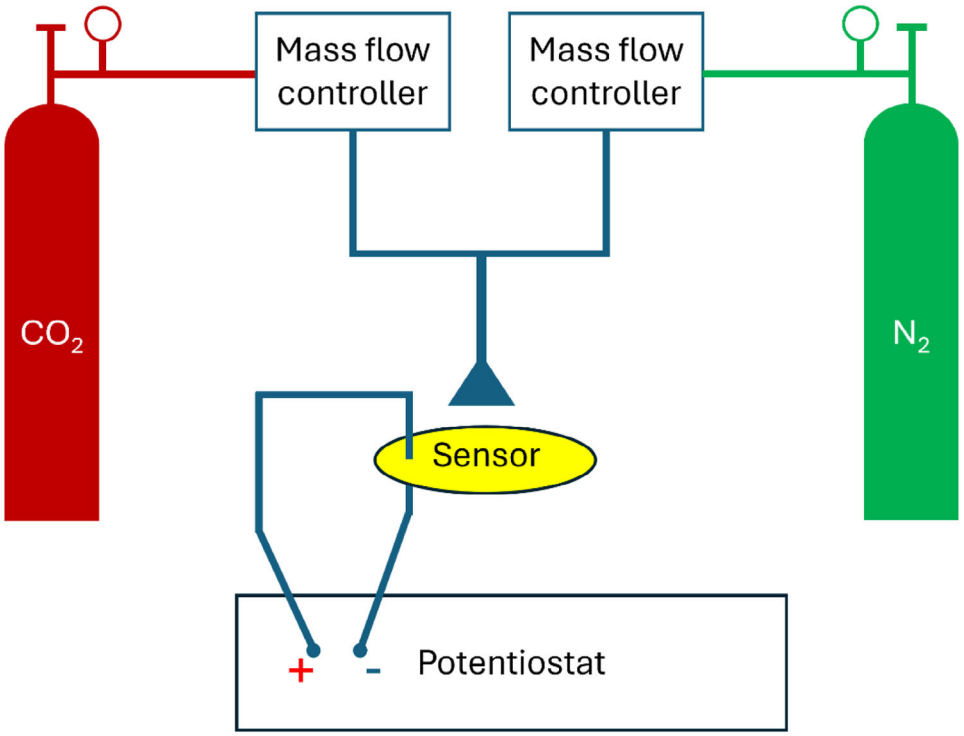

SCHEME 1 | Scheme of electrochemical measurement for testing PIM-1_ ChoIm based membrane.

desorption to be observed over an additional 8 h, and the mass was recorded again at minute 1260. The CO_2 absorption (Abs%) and desorption (Des%) values were calculated using the following equations:

$$Abs\ (\%) = 100 * \frac{(final\ weight - initial\ weight)}{(initial\ weight)} \quad (1)$$

$$Des\ (\%) = 100 * \frac{(desorbed\ weight - initial\ weight)}{(initial\ weight)} \quad (2)$$

All values are reported with three significant figures.

2.5 | Electrochemical Measurements

Electrochemical measurements were carried out using a VMP-3 system (Biologic), equipped with potentiostat/galvanostat modules and frequency response analyzers for performing electrochemical impedance spectroscopy (EIS). The EIS tests were conducted across a frequency range of 10^6–10^{-2} Hz, with ten points recorded per frequency decade and a signal amplitude of 5 mV. Open circuit voltage (OCV) measurements were also performed to assess the electrochemical cell's response during gas absorption, with a voltage resolution of 1 mV. All experiments were conducted in a commercially available ECC-Air test cell (El Cell GmbH), designed to facilitate electrochemical measurements while allowing a gas stream to be introduced into the sample chamber as summarized in Scheme 1.

The response time (T90) is defined as the time required to reach 90% of the total voltage variation upon CO_2 exposure, while the recovery time corresponds to the time required to return to 10% of the baseline signal under N_2 flow. The reported response and recovery times represent the average of at least three independent cycles, with an estimated variability below ±5%. The gas flow rate during sensing tests was fixed at 20 mL min^{-1} unless otherwise specified. All electrochemical measurements were performed at controlled room temperature (25 ± 1°C).

3 | Results

3.1 | Physico-Chemical Properties of ChoIm and PIM-1_ ChoIm Based Membrane

The DES was first characterized as a pure component prior to further analysis. The pH of a 0.01 M aqueous solution prepared in deionized water was 9.2, consistent with the presence of imidazole and its intrinsic basicity. The density of the DES in this formulation was 1.1025 g cm^{-3} and a viscosity of up to 900 mPa s.

As shown in Figure 2, it is possible to determine the anodic and cathodic limiting potentials by arbitrarily imposing a cutoff current density over which the sample starts to deteriorate. In this case the maximum current rate was set at 0.1 mA cm^{-2} finding a ESW comprised between −0.6 and 0.8 V [48].

As shown in CV reported in Figure 3, it is evident that once the anodic potential exceeds +0.5 V, an irreversible degradation peak starts to appear. This phenomenon becomes particularly pronounced when the cell is polarized up to +1 V.

FT-IR (ATR mode) spectroscopy was performed on blended PIM-1 membranes to prove the successful introduction of ChoIm within the PIM-1 based films. As reported in Figure 4, the PIM-

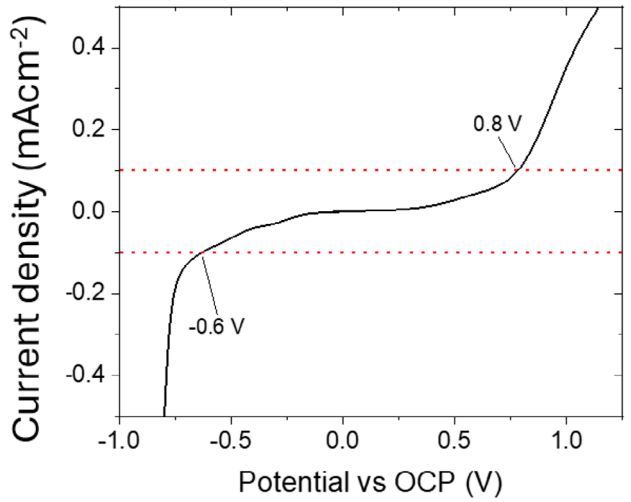

FIGURE 2 | Linear sweep voltammetry of ChoIm at 5 mV s^{-1} on a Pt electrode.

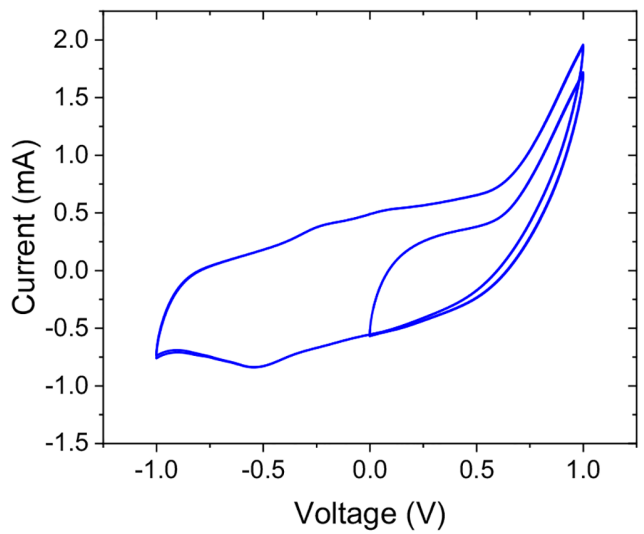

FIGURE 3 | Cyclic voltammetry of ChoIm at 5 mV s^{-1} in device configuration with 2 commercial gas diffusion electrodes.

1 spectrum (black line) displays the typical peaks of the polymer [49–52, 21]. In the high-frequency region, the absorption band at 3055 cm^{-1} is indicative of aromatic ν_{C-H} vibrations, characteristic of substituted aromatic rings [53–55]. In the aliphatic region, three main peaks are detected at 2956, 2926, and 2866 cm^{-1}, corresponding to the ν_{CH3} and ν_{CH2} groups, along with a δ_{C-H} at 1453 cm^{-1}. A sharp and distinct signal at 2240 cm^{-1} is attributed to the $\nu_{C\equiv N}$ of nitrile functionalities, a diagnostic signal of PIM-1 [53–56]. The aromatic ring $\nu_{C=C}$ was associated to the peak at 1608 cm^{-1}, while additional absorptions at 1212, 876, and 754 cm^{-1} correspond to in-plane and out-of-plane δ_{C-H} deformations of substituted aromatics [53]. Furthermore, absorption bands appear at 1312, 1292, 1267, and 1109 cm^{-1} which are characteristic of ether linkages ν_{C-O-C} formed through the SNAr polymerization process [53, 54].

As shown in Figure 4 (blue line), ChoIM showed a broad band in the 3220−3026 cm^{-1} range due to the presence of hydroxylic

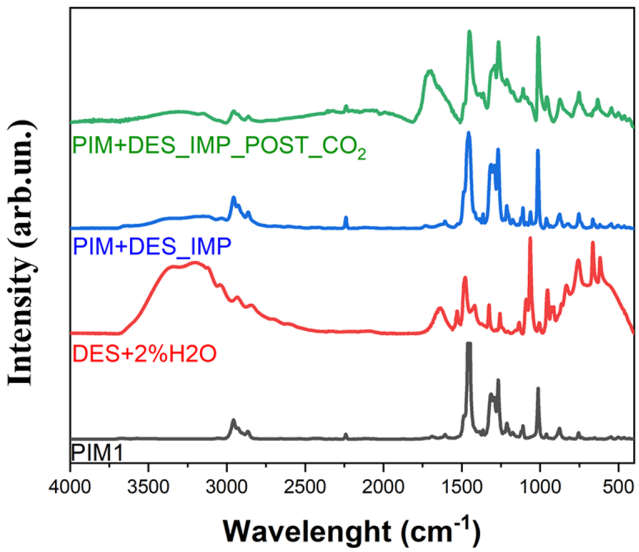

FIGURE 4 | ATR-FTIR of PIM-1 (black line), ChoIm (red line) and PIM-1_ ChoIm prior (blue line) and after CO_2 exposure (green line) in the range from 500 up to 4000cm^{-1}.

functionalities and amine ones entangled into a hydrogen bond network while n_{CH} peak centered at 2963 cm^{-1} and the n_{C-O} centered at around 1084 cm^{-1} were the choline cations and a broad bad centered 1639 cm^{-1} due to the adsorbed CO_2 [57]. Other diagnostic bands were detectable in the range between 1200 and 880 cm^{-1} due to both C—O and C—N bond vibrations, ρ_{CH} at 1481 cm^{-1} and ν_{C-O-C} [58].

The presence of imidazole was confirmed by the ν_{N-H} of at 3407 cm^{-1} [59], the peaks in the region between 3000−3250 cm^{-1} region due to unsaturated ν_{C-H} of the imidazole ring [60], of the imidazole ring and the imidazole ring breathing vibrations ranging from 1500 to 1620 cm^{-1} range [61].

As shown in Figure 2 (blue line), the incorporation of the ChoIm into the PIM-1_ChoIm blend is evidenced by the appearance of a broad absorption band in the 3690–3092 cm^{-1} region. This feature arose from hydrogen-bonding interactions involving the imidazole nitrogen atoms as well as the –OH groups of choline chloride. This band was clearly observed in the neat ChoIm spectrum but was absent in PIM-1 confirming the presence of ChoIm within the polymer matrix. In the aromatic region, the characteristic aromatic $\nu_{C=C}$ at 1607 cm^{-1} was detectable after DES introduction together with a broader contribution due to imidazole cantered at 1639 cm^{-1} and a band at 1730 cm^{-1} due to the formation of a carbamate species between the imidazole moiety of ChoIm in presence of CO_2 [62]. The absence of carbamate related band in the neat ChoIm suggested that ChoIm may be more reactive or less stable when confined within the PIM-1 matrix. Following blending, an additional DES-related band at 1530 cm^{-1} became appreciable and it was due to the symmetric deformation of NH_3^+ groups supporting successful incorporation of the DES component. Moreover, characteristic ChoIm bands at 1603 and at 1089 cm^{-1}, associated with ν_{C-O} and ν_{C-N} stretching modes also appeared in the blend and were entirely absent in pure PIM-1 further supporting the integration of the ChoIm within the polymer network. The band centred

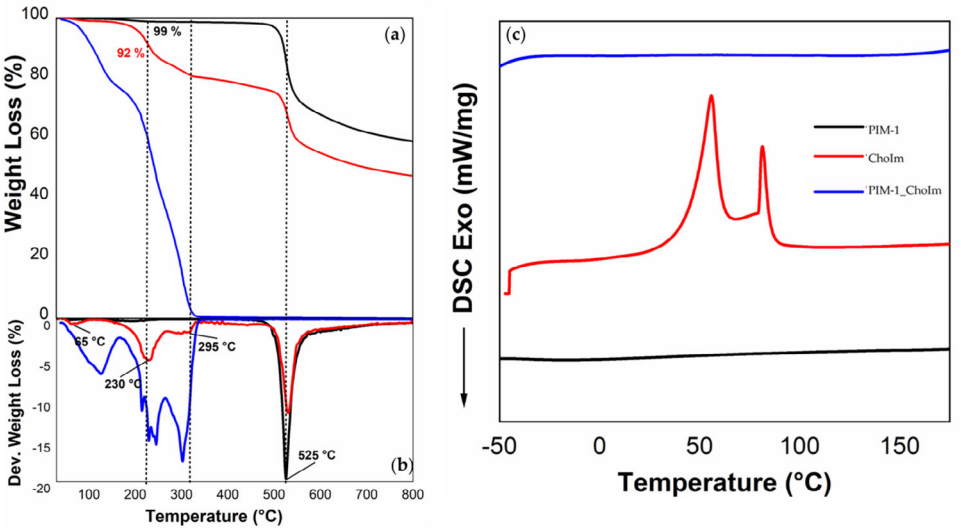

FIGURE 5 | Summary of (a) TGA (b) derivative weight loss curves and (c) DSC curves of PIM-1 (black line), ChoIm (blue line) and PIM-1_ChoIm (red membrane).

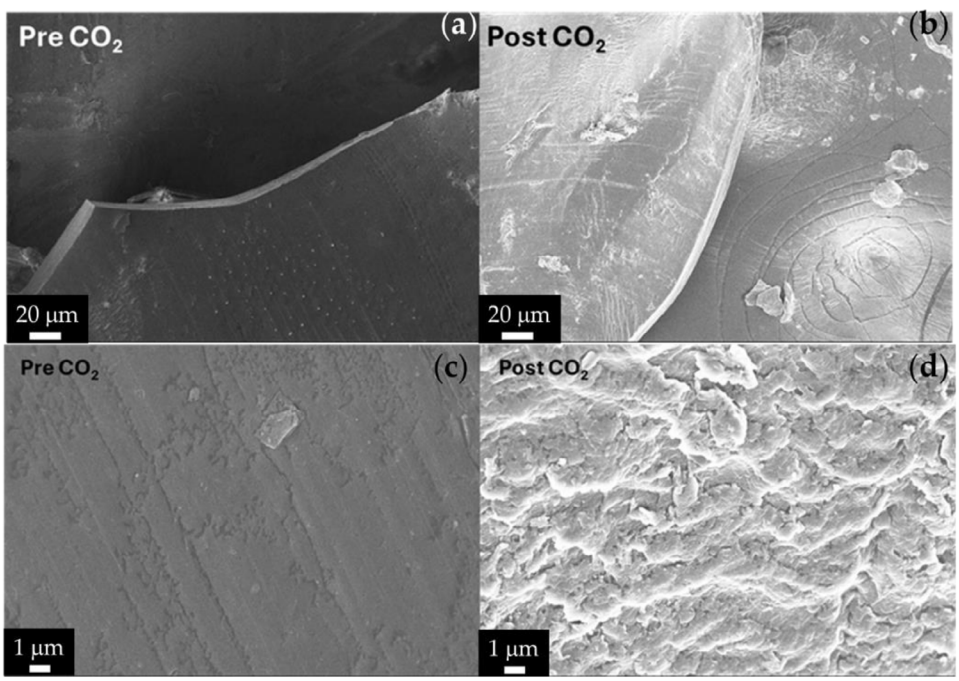

FIGURE 6 | FESEM images of PIM-1 membrane pre and post CO_2 exposure (a,b respectively) compared with PIM-1_ChoIm pre and post CO_2 exposure (c,d).

at 1730 cm^{-1} rising after CO_2 exposure strongly supports the formation of carbamate species through the interaction between CO_2 and imidazole groups accordingly with previously reported imidazole-based systems [63].

TGA was performed on the materials to assess both the degradation pattern and thermal properties of the fabricated membranes and ChoIm [64] as shown in Figure 5.

In Figure 5a,b, the TGA curve showed that the pure PIM-1 membrane (black line) underwent a single thermal degradation event at approximately 525°C [65].

The ChoIm (Figure 5a,b, red line) degraded in a single step with decomposition and evaporation of the IL with a maximum degradation rate at almost 300°C.

PIM-1_ ChoIm (Figure 5a,b, blue line) showed two distinct degradation stages, one between 200°C and 425°C and another between 510–520°C, corresponding to the degradation of ChoIm and PIM-1, respectively. A minor weight loss observed below 100°C was attributed to the loss of CO_2 absorbed from the atmosphere as shown by FT-IR spectra. As shown in Figure 5c, PIM-1 and PIM-1_ChoIl did not show any significant phase or kinetic transition [44] while ChoIm showed two endothermic

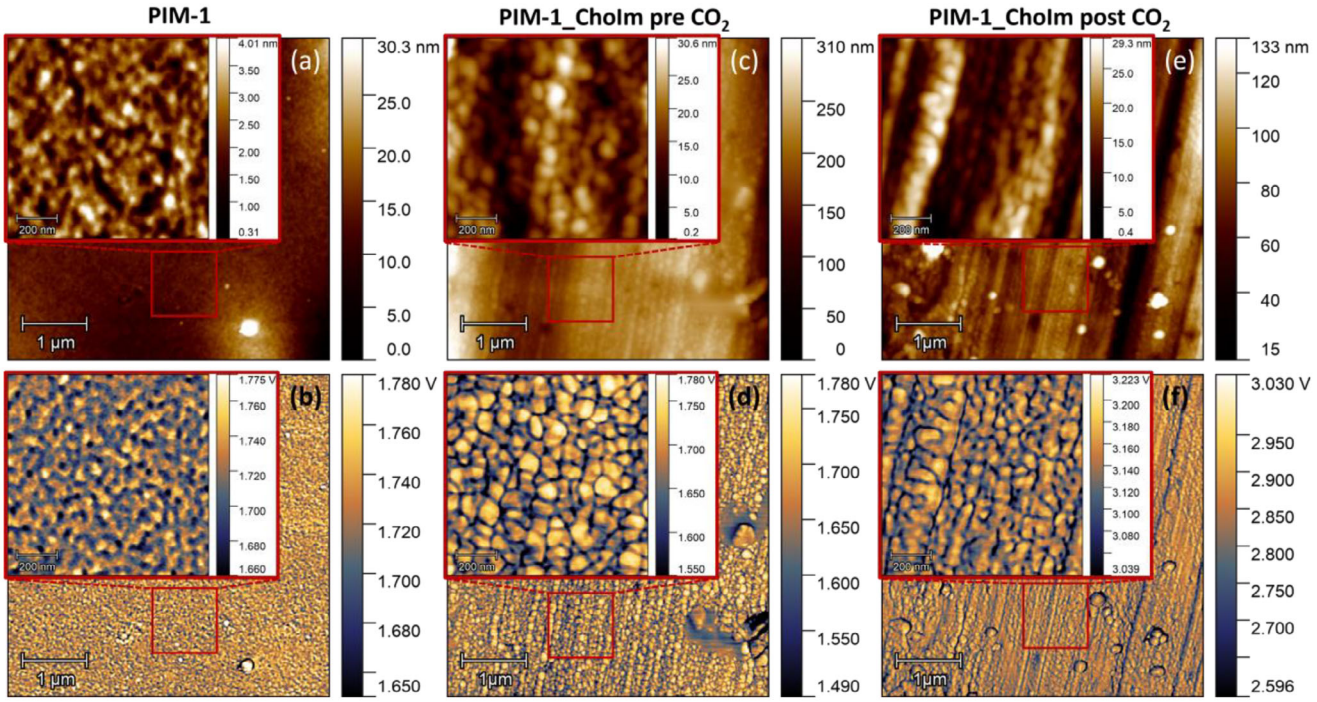

FIGURE 7 | AFM images of the PIM-1 membrane before CO_2 exposure (a,b), and of the PIM-1_ChoIm membrane both before (c,d) and after (e,f) CO_2 exposure. Panels (a,c,e) are the topography maps, panels (b,d,f) are the phase contrast images. Insets to each panel display selected areas under high magnification.

phase changes at 56°C and 82°C. The first one could be associated to the melting of DES while the second one is related the melting of release imidazole while the pure one shows a melting point at around 87°C–90°C [66].

The morphology of the PIM-1_ChoIm prior and after CO_2 exposure was evaluated though FESEM analysis as shown in Figure 6.

PIM-1 membranes (Figure 6a,b) showed smooth surfaces before and after CO_2 exposure, while PIM-1_ChoIm after CO_2 exposure (Figure 6d) showed the presence of rough surfaces due to the incorporation of CO_2 into ChoIm with a volume shrinkage compered to neat one (Figure 6c).

The FESEM results were further corroborated by means of the AFM investigation summarized in Figure 7.

The topography of the pure PIM-1 membrane (Figure 7a) shows a flat surface with sub-nanometric corrugation (background rms roughness ~0.7 nm) and no preferential orientation, over which globular particles (thickness 8–60 nm; lateral size 80–200 nm) are randomly scattered. Despite the flatness of the background, the phase image (Figure 5b) displays an observable contrast, indicating a texturing of the surface mechanical properties of the membrane likely arising from its microporosity.

DES impregnation markedly alters the membrane nanostructure. The topography map of the PIM-1_ChoIm membrane before CO_2 exposure (Figure 7b) displays a clear granular structure (grain thickness 10–15 nm; grain lateral size 20–60 nm) that was organized in a long-range striped pattern which strongly increases the surface corrugation (background rms roughness ~14 nm).

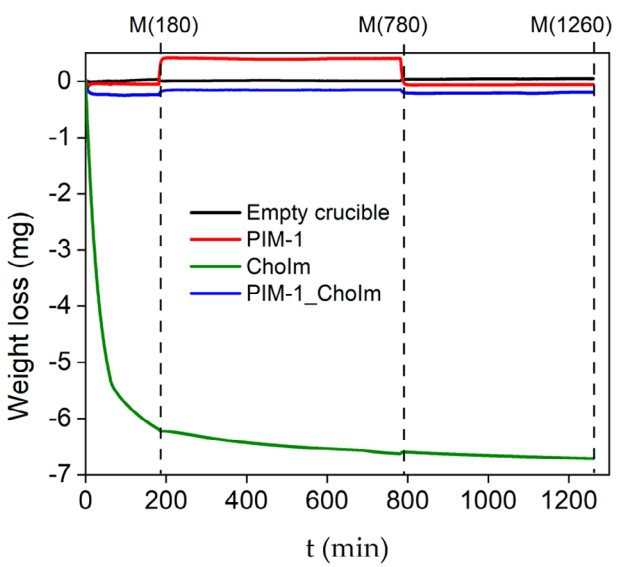

FIGURE 8 | Qualitative CO_2 absorption and weight loss patterns across the different membrane compositions: pure PIM-1, PIM-1_ ChoIm, and ChoIm highlighting the efficiency and reversibility of CO_2 capture for each sample.

The corresponding phase image (Figure 7c) is dominated by the grain boundaries, which are extremely well-defined and clearly separate each individual grain.

The impact of CO_2 exposure is more subtle than that of DES impregnation. In the topography map of the PIM-1_ChoIm membrane after CO_2 exposure (Figure 7e), the same granular structure can be observed in the background, albeit with a

TABLE 2 | Data summary of CO_2 absorption and desorption data for pure PIM-1, PIM-1_ChoIm and pure ChoIm. Weight changes and the efficiency of CO_2 capture and release.

Sample	Mass (mg)			Abs (%)	Des (%)
	Initial min [a]	Final [b]	Desorbed [c]		
PIM1	25.8746	26.3355	25.8662	1.78128	−1.78201
PIM-1_ChoIm	10.0632	10.14911	10.10471	0.8537	−0.43748
ChoIm	23.7958	23.3491	23.2631	−1.87722	−0.36832

[a]Initial: Mass of the sample measured after purging with N_2 to eliminate moisture, CO_2, and any other adsorbed gases prior to testing.
[b]Final: Mass of the sample recorded following CO_2 adsorption.
[c]Desorbed: Mass of the sample obtained after removing the adsorbed CO_2 by purging again with N_2.).

slight reduction in the grain thickness (grain thickness 5–12 nm; grain lateral size 20–70 nm); the striped pattern also becomes more observable (corresponding to a slight increase in the rms roughness ~15 nm). Interestingly, the phase contrast image (Figure 7f) is still dominated by the grain boundaries, which are however less well-defined than before CO_2 exposure, suggesting a partial merging between the grains. Both observations are consistent with volume shrinkage induced by CO_2 absorption, as also observed in FESEM.

Additionally, large agglomerates (thickness 40–100 nm; lateral size 300–700 nm) can be observed in the topography maps of both the PIM-1_ChoIm membranes before and after CO_2 exposure. The absence of phase contrast between these agglomerates and the background suggested that they likely originate from membrane extrusion and not from phase separation or surface contamination.

PIM-1, ChoIm and PIM-1_ChoIM were tested in order to verify their ability to sample adsorbed CO_2 as reported in Figure 8.

As shown in Figure 8 and summarized in Table 2, N_2 was used as purging gas to eliminate water, CO_2, and other gases adsorbed on the sample prior to testing. The samples initial mass (column: Initial) was recorded before the purging process. Next, CO_2 adsorption was carried out, and the final mass after adsorption (column: Final) was measured. Following this, the mass after desorption (column: Desorbed) was recorded after using the purging gas to remove the adsorbed CO_2. The pure PIM-1 membrane demonstrated excellent CO_2 absorption and almost complete desorption, returning to a mass very close to its initial value. This performance underscores the efficiency of PIM-1 in reversibly adsorbing and releasing CO_2.

In contrast, the PIM-1_ChoIm sample exhibited relatively low CO_2 uptake and a pronounced weight loss upon desorption. This behavior is likely associated with the partial volatilization of the ionic liquid, which decomposes into choline and imidazole, suggesting weak interactions between the polymer matrix and the deep eutectic solvent (DES).

A comparable trend was observed for the PIM-1_ChoIm blend; however, in this case, a higher CO_2 uptake accompanied by a smaller weight loss was recorded. These results indicate that increasing the DES content enhances CO_2 sorption capacity, although some degree of instability persists.

The impregnated PIM-1_ChoIm sample, on the other hand, displayed excellent CO_2 uptake comparable to that of pristine PIM-1, along with improved reversibility during the adsorption–desorption cycles. This behavior points to a stronger interaction between the polymer and the ionic liquid when the latter is introduced through impregnation.

Finally, the pure ChoIm exhibited remarkably high CO_2 adsorption, which continuously increased over time without reaching a saturation plateau, followed by negligible weight loss during desorption. Such behavior can be attributed to diffusion constraints within the DES droplets; unlike thin membranes, the droplet's considerable thickness, combined with its surface tension and high viscosity, hinders uniform CO_2 release, leading to slow and inefficient desorption [67].

The negative absorption values observed for the pure ChoIm sample are attributed to mass loss phenomena occurring during the experiment, likely related to partial volatilization and structural rearrangement of the DES under gas flow conditions. This behavior is consistent with its physicochemical properties including both high viscosity and dynamic hydrogen-bonding network and does not indicate calculation errors.

3.2 | Electrochemical Characterization of PIM1-Based Membranes

The membranes impedance has been analyzed, and the EIS plot displays characteristics typical of an ionic conductive membrane. Specifically, it shows a semicircle in the high frequency region and a bent line in the low frequency region (Figure 9 a black dots). The data was fitted using the equivalent circuit reported in the figure (see Figure S1) with the resulting curve (see Figure S2, red curve) with R1 that describes the ESR, R2 represents the surface film resistance, while the charge-transfer resistance is R3. A Warburg element is included to represent diffusion behavior at low frequencies, while the Constant Phase Elements (CPE) reflects non-ideal capacitive behavior [68]. Evaluating the high frequency resistance (obtained from the Nyquist plot at the phase angle 0) it is possible to compute the membrane's conductivity by using Equation (3)

$$\sigma = \frac{1}{R_{hf}}\ k = 96,97 \mu S \cdot cm^{-1} \quad (3)$$

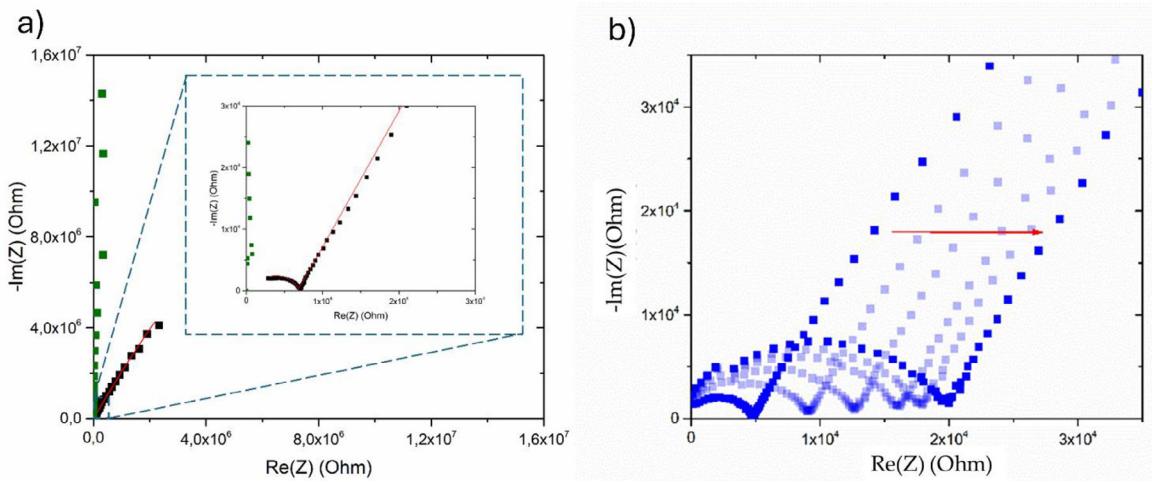

FIGURE 9 | Comparison between (a) EIS of PIM-1_ChoIm (green dots) and the one of wetted PIM-1 (black dots) NYQUIST and (b) of wetted membrane without any gas interaction (black) and membrane post CO_2 interaction (red).

where k is the cell constant (d/A). Although this equation is commonly used to evaluate membrane conductivity, it is worth noting that it is an approximation, as the R_{hf}value includes the membrane resistance, electronic cell resistance, and interfacial contact resistance [69].

As shown in Figure 9b, PIM- samples were analyzed under CO_2 gas flow to evaluate the membrane's eventual sensibilities to CO_2 adsorption. We found that only the wetted sample showed a remarkable impedance spectra variation both in real and imaginary part variations, as reported in Figure 9b. In this system, carbon dioxide has been chemisorbed by the ChoIm presents in the membrane altering the electrochemical behavior of the sample. This change is quite evident by monitoring EIS measurements during CO_2 exposure. However, this change cannot be reversed, as the initial spectroscopy cannot be restored either by using nitrogen or temperature as regenerative methods (see Figure S2). Hence, EIS monitoring is not suitable for the CO_2 detection with the present system.

Accordingly, the CO_2 sensing using PIM-1_ChoIm was evaluated through OCV measurements as reported in Figure 8. Here it is depicted the impact of a 20 mL min^{-1} flow of CO_2 on the OCV, showcasing an approximate variation of 20 mV. In particular, when the CO_2 interacted with soaked membrane, the device voltage initially underwent to a slight increment, followed by a significant drop. This OCV shift can be completely reversed by introducing a nitrogen flow of 100 mL min^{-1} for 5 min which restored the voltage to its baseline. Furthermore, all the voltage fluctuations were attributable to the interaction between the sample and the gas stream. As shown in Figure 10, the behavior of the voltage response was highly reproducible, maintaining a steady and predictable cycle for over 100 repetitions without significant deviations.

The discrepancy between the irreversible behavior observed during EIS measurements and the fully reversible OCV response can be explained by the different physical processes probed by the two techniques [70]. EIS reflects bulk ionic transport and interfacial charge transfer which are strongly affected by the formation of carbamate/bicarbonate species within the DES

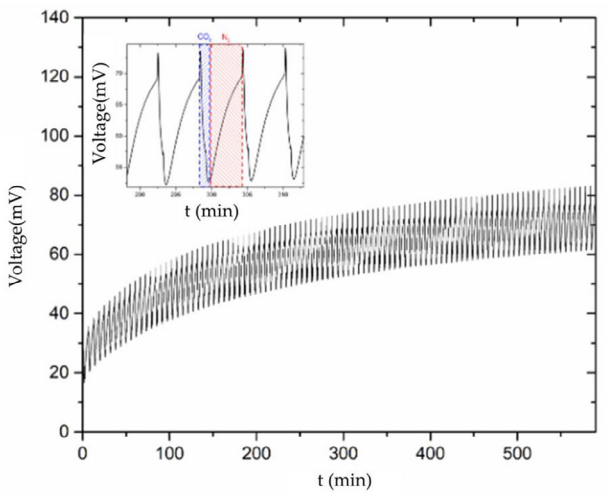

FIGURE 10 | Repeatable voltage swing of the OCV during the alternate flushing of CO_2 and N_2 at 25°C.

phase leading to persistent modifications of the conduction pathways. OCV measurements probe near-equilibrium surface processes where adsorption/desorption equilibria are rapidly restored under nitrogen flow.

After those first experiments, we decided to perform deeper analysis on the membrane behavior under different working conditions. Results are reported in Figure 11. In these tests, the main interest was to understand how the system reacts when subjected to different CO2 concentrations in an incoming gas flow over an extended duration.

As reported in picture 11 a, a voltage variation is clearly induced by the incoming gas stream and the peak-to-peak change is correlated with the carbon dioxide content in the flow. For this system, the detection limit was empirically determined as 2% CO_2, as this is the lowest concentration which produces an appreciable change in the OCV of the membrane. By increasing the amount of carbon dioxide in the incoming stream, overall ΔV changes according to a logarithmic trend, as reported in Figure 9b. In

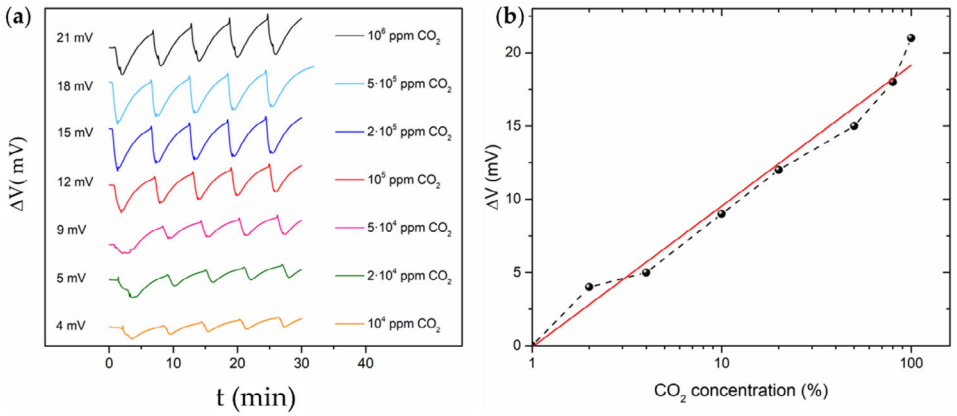

FIGURE 11 | OCV measurements of repeated CO_2 adsorption/desorption tests at 25°C with different CO_2 concentrations (a,b) sensitivity curve.

TABLE 3 | Main electrochemical performances of PIM-1_ChoI for CO_2 detection.

CO_2 (%)	Response time (s)	Recovery time (s)
100	29	240
80	34	236
50	34	236
20	40	232
10	43	228
4	40	221
2	51	214

Earth's atmosphere, carbon dioxide is present at approximately 420 ppm [71], and it becomes toxic at concentrations above 5% [72]. The proposed sensor is suitable for monitoring environments and detecting CO_2 concentrations that could pose a risk to human health. The sensor sensitivity was determined by fitting the experimental data with the equation $\Delta V = 9.6 \cdot \log(CO_2\%) - 0.09$ The sensitivity is defined as the multiplicative factor of the log function, which in this case is 9.6 mV dec$(\%CO_2)^{-1}$ as summarized in Table 3.

The activity of PIM-1_ChoI toward CO_2 sensing can be due to a first interaction with choline chloride and imidazole anions through CO_2 aligns preferentially with the π rich area of imidazole ring and with the dipolar fields created by the choline head and tail group [73] increasing CO_2 concentration near the electrode interface.

As CO_2 diffuses into the imidazole-rich microdomains, the nitrogen atom of the imidazole ring can attack the electrophilic carbon of CO_2 forming a zwitterionic intermediate that led to the formation imidazolyl carbamate species as proved by IR reported in Figure 4 (green line). In the presence of trace water, a competing pathway generates bicarbonate through hydration of CO_2 with the proton transfer to imidazole forming imidazolium [74]. These equilibria can create a dynamic balance between free dissolved CO_2, carbamate and bicarbonate species while the hydrogen bond network of the DES reorganizes around these species with imidazole and chloride adjusting their interactions to stabilize the intermediates and modulate the local diffusivity Figure 12.

Most meaningful parameters of PIM-1_ChoIm based sensor and those of other literature reported sensors are reported and compared in Table 4. Compared to other reported sensors, this work has the fastest response time (90s) and works properly in the range where carbon dioxide becomes lethal for human health. It was flexible and able to work at room temperature and provides good reversibility. Altogether, the fabricated sensor offered superior features that overcome the challenges that existed in current CO_2 sensing devices.

In Table 4, sensitivity parameter has been included and a compared with polymer-based and PIM-based CO_2 sensors has been expanded.

4 | Conclusions

This work reported the successful design and assessment of an innovative potentiometric CO_2 sensor based on PIM-1 membranes incorporating ChoIm. By combining the intrinsic microporosity of PIM-1 with the remarkable CO_2 absorption capability of the imidazolate-based deep eutectic solvent, a highly efficient sensing platform has been achieved, exhibiting improved sensitivity and selectivity toward carbon dioxide. The findings highlight the promising applicability of this hybrid material system in a broad range of gas sensing technologies.

The PIM-1_ChoIm membranes exhibited excellent robustness and stability, effectively mitigating the issue of ionic liquid leakage that often affects conventional gas sensors. This enhanced stability, together with the high efficiency in CO_2 adsorption and desorption, underscores their potential for long-term deployment in environmental and industrial monitoring applications. Moreover, TGA and FTIR analyses verified that the membranes preserve both their structural integrity and functional properties over prolonged operation, even when exposed to fluctuating CO_2 concentrations.

Furthermore, the versatility of the PIM-1_ ChoIm imidazolate membranes broadens their potential applications to diverse contexts such as air quality management and industrial process monitoring. The sensors exhibited remarkable performance in detecting CO_2 across a wide range of concentrations, underscoring their capability to contribute meaningfully to environmental sus-

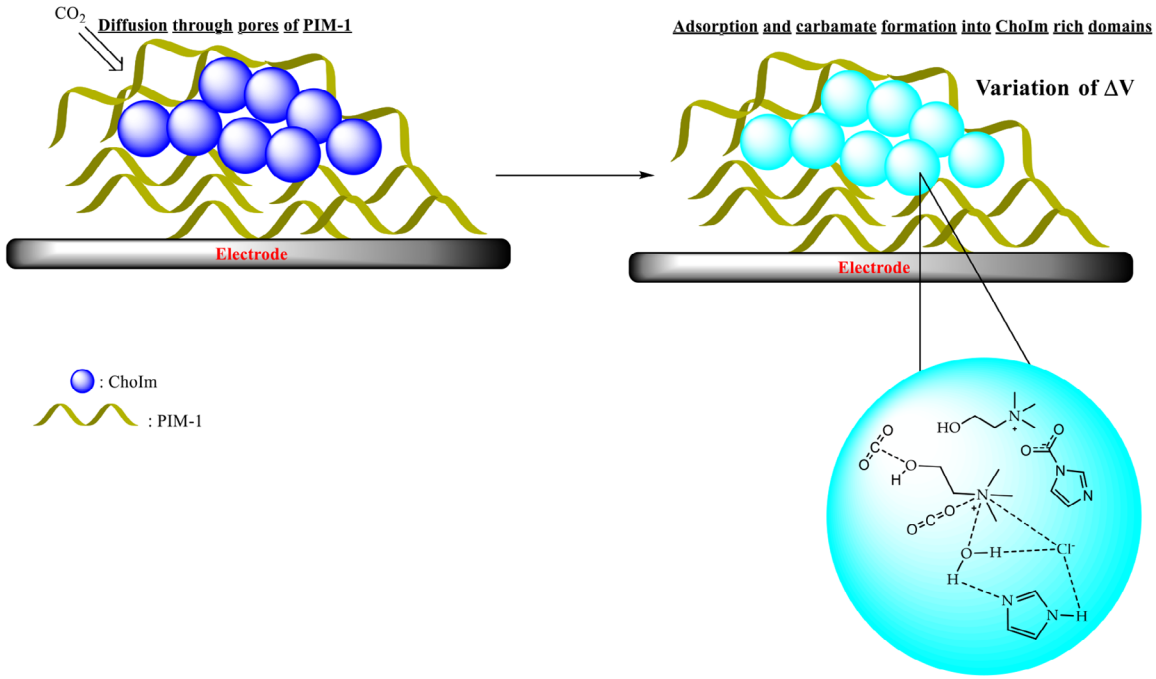

FIGURE 12 | Hypothetical interaction mechanism of CO_2 on PIM-1_ChoI during sensing.

TABLE 4 | Sensor performance under different gas conditions.

Sensing material	Detection range (ppm)	Response time (s)	Recovery time (s)	Operating temperature (°C)	Reversible	Flexible
This work	2×10^4–10^6	29	240	25	Yes	Yes
PEI- CNTs [75]	200–1000	600	600	rt	Yes	Yes
PEDOT/PSS, graphene [76]	400–4200	NA	NA	50 and 60	No	Yes
PEI-PANI [77]	50–5000	440 ± 313	601 ± 292	rt	Yes	No
SPES/e-MWCNTs [78]	500–5000	480–840	1620	rt	Yes	No
PEI/PEG [79]	200–25×10^4	251	300	rt	Yes	No
SPEEK-5/d-MWCNTs [80]	500–5000	250–665	1322–1622	rt	Yes	No

tainability and safety. Their efficient CO_2 adsorption–desorption behavior makes these membranes particularly well suited for real-time monitoring systems that demand rapid response and high sensitivity.

This study also paves the way for future research, suggesting that the exploration of deep eutectic solvents or polymer matrices could further enhance the selectivity and sensitivity of gas sensors toward different analytes. Such efforts may ultimately lead to the development of a new generation of advanced, sustainable, and high-performance gas sensors designed for specific industrial and environmental applications.

In summary, the PIM-1_ChoIm membranes represent a significant advancement in gas sensing technology, offering a reliable and effective platform for CO_2 detection. They contribute to the broader goal of developing sustainable materials and technologies for environmental monitoring. The role of PIM-1 is not limited to mechanical support but is fundamental in enhancing gas transport. Its intrinsic microporosity provides interconnected free volume elements that facilitate CO_2 diffusion toward the active DES phase. This confinement effect improves both adsorption kinetics and desorption efficiency compared to bulk DES systems in which transport limitations are dominant.

The outcomes of this work establish a strong foundation for the continued innovation of polymer–ionic liquid composite sensors, highlighting their critical role in enhancing gas sensing performance and addressing pressing environmental challenges. The combination of intrinsic microporosity and reactive DES chemistry enables a unique sensing mechanism, in which fast gas transport and reversible chemical interaction coexist, resulting in a synergistic improvement of both response time and reversibility compared to conventional systems.

Acknowledgements

Open access publishing facilitated by Politecnico di Torino, as part of the Wiley - CRUI-CARE agreement.

Funding

This research was partially funded under the National Recovery and Resilience Plan (NRRP), Mission 4 "Education and Research"—Component 2 "From research to business"—Investment 3.1 "Fund for the realization of an integrated system of research and innovation infrastructures"—Call for tender No. n. 3264 of 28/12/2021 of Italian Ministry of Research funded by the European Union—NextGenerationEU—Project code: IR0000027, Concession Decree No. 128 of 21/06/2022 adopted by the Italian Ministry of Research, CUP: B33C22000710006, Project title: iENTRANCE. This study was carried out within the Agritech National Research Center and received funding from the European Union Next-GenerationEU (PIANO NAZIONALE DI RIPRESA E RESILIENZA (PNRR)—MISSIONE 4 COMPONENTE 2, INVESTIMENTO 1.4 – D.D. 1032 June 17, 2022, CN00000022). Furthermore, authors wish to thank European Union for the financial support through the Next Generation EU- projects "Nord Ovest Digitale E Sostenibile-NODES" (PNRR, D.D. n.1054 June 23, 2022), NEST "Network for Energy Sustainable Transition-NEST"(PE0000021, D.D. n.341 March 15, 2022), PRIN 2022 PNRR project "Continuous THERmal monitoring with wearable mid-InfraRed sensors" (P2022AHXE5), and Project PNC 0000001 D3 4 Health,—CUP B83C22006120001, The National Plan for Complementary Investments to the NRRP, Funded by the "European Union—NextGenerationEU". Authors also acknowledge Ministero dello Sviluppo Economico (MISE) and Ministero della Transizione Ecologica (MITE) for financial support. These results are part of a project that has received funding from the European Research Council (ERC) under the European Union's ERC Starting Grant agreement "CO2CAP" No. 949916. This manuscript reflects only the authors' views and opinions, neither the European Union nor the European Commission can be considered responsible for them.

Conflicts of Interest

The authors declare no conflicts of interest.

Data Availability Statement

The data that support the findings of this study are available from the corresponding author upon reasonable request.

References

1. R. Svigelj, R. Toniolo, C. Bertoni, and A. Fraleoni-Morgera, "Synergistic Applications of Graphene-Based Materials and Deep Eutectic Solvents in Sustainable Sensing: A Comprehensive Review," *Sensors* 24 (2024): 2403, https://doi.org/10.3390/s24082403.

2. C. M. Brett, "Deep Eutectic Solvents and Applications in Electrochemical Sensing," *Current Opinion in Electrochemistry* 10 (2018): 143–148, https://doi.org/10.1016/j.coelec.2018.05.016.

3. C. M. Brett, "Perspectives for the Use of Deep Eutectic Solvents in the Preparation of Electrochemical Sensors and Biosensors," *Current Opinion in Electrochemistry* 45 (2024): 101465, https://doi.org/10.1016/j.coelec.2024.101465.

4. T. El Achkar, H. Greige-Gerges, and S. Fourmentin, "Basics and Properties of Deep Eutectic Solvents: A Review," *Environmental Chemistry Letters* 19 (2021): 3397–3408.

5. Y. Liu, J. B. Friesen, J. B. McAlpine, D. C. Lankin, S. N. Chen, and G. F. Pauli, "Natural Deep Eutectic Solvents: Properties, Applications, and Perspectives," *Journal of natural products* 81 (2018): 679–690, https://doi.org/10.1021/acs.jnatprod.7b00945.

6. T. Negi, A. Kumar, S. K. Sharma, et al., "Deep Eutectic Solvents: Preparation, Properties, and Food Applications," *Heliyon* 10 (2024): 1–10.

7. B. B. Hansen, S. Spittle, B. Chen, et al., "Deep Eutectic Solvents: A Review of Fundamentals and Applications," *Chemical Reviews* 121 (2020): 1232–1285, https://doi.org/10.1021/acs.chemrev.0c00385.

8. A. P. Abbott, G. Capper, D. L. Davies, H. L. Munro, R. K. Rasheed, and V. Tambyrajah, "Preparation of Novel, Moisture-stable, Lewis-acidic Ionic Liquids Containing Quaternary Ammonium Salts With Functional Side Chains," *Chemical Communications* 37 (2001): 2010–2011, https://doi.org/10.1039/b106357j.

9. J. Wu, Q. Liang, X. Yu, et al., "Deep Eutectic Solvents for Boosting Electrochemical Energy Storage and Conversion: A Review and Perspective," *Advanced Functional Materials* 31 (2021): 2011102, https://doi.org/10.1002/adfm.202011102.

10. D. Fuchs, B. C. Bayer, T. Gupta, et al., "Electrochemical Behavior of Graphene in a Deep Eutectic Solvent," *ACS Applied Materials & Interfaces* 12 (2020): 40937–40948, https://doi.org/10.1021/acsami.0c11467.

11. G. Gavello, G. Tofani, D. De Fazio, et al., "Facile Synthesis of Palladium Hydride via Ionic Gate-driven Protonation Using a Deep Eutectic Solvent," *Journal of Molecular Liquids* 420 (2025): 126826, https://doi.org/10.1016/j.molliq.2024.126826.

12. N. Arab, L. Fotouhi, A. Salis, and P. S. Dorraji, "An Amplified Electrochemical Sensor Employing a Polymeric Film and Graphene Quantum Dots/Multiwall Carbon Nanotubes in a Deep Eutectic Solvent for Sensitive Analysis of Paracetamol and 4-aminophenol," *New Journal of Chemistry* 44 (2020): 15742–15751, https://doi.org/10.1039/D0NJ03371E.

13. M. Madagalam, M. Bartoli, S. Carrara, and A. Tagliaferro, "$ZnM_xFe_{2-x}O_4$ (M = Cr, Bi) Nanoparticles-Modified Electrochemical Sensors: Effect on Sensitivity and First-Order Kinetic Rate Constant," In *2023 IEEE BioSensors Conference (BioSensors 2023) – Proceedings*, (IEEE, 2023).

14. M. Madagalam, M. Bartoli, S. Carrara, and A. Tagliaferro, "$ZnCr_2$−xFe_xO_4 Nanoparticles-Modified Electrochemical Sensors: A Comparative Study," In *Proceedings of IEEE Sensors*, (IEEE, 2023).

15. M. Madagalam, M. Bartoli, M. Rosito, et al., "Unraveling the Effect of the Chemical and Structural Composition of $Zn_xNi_{1-x}Fe_2O_4$ on the Electron Transfer at the Electrochemical Interface," *Small Structures* 4 (2023): 2300163.

16. M. Madagalam, M. Bartoli, M. Rosito, et al., "Effect of Cr Substitution in $ZnFe_2O_4$ Nanoparticles on the Electron Transfer at Electrochemical Interfaces," *Materials Research Bulletin* 183 (2025): 1–13.

17. M. Madagalam, M. Bartoli, A. Tagliaferro, and S. Carrara, "Bismuth-Nanocomposites Modified SPCEs for Non-Enzymatic Electrochemical Sensors," *IEEE Sensors Journal* 21 (2021): 11155–11162, https://doi.org/10.1109/JSEN.2021.3059278.

18. M. Madagalam, F. Franceschini, C. Fernandes, et al., "Comparative Study of ZnO and $ZnFe_2O_4$ Microparticle and Nanoparticle-Based Screen-Printed Electrodes in pH Sensing," *IEEE Sensors Journal* 25 (2025): 10602–10612, https://doi.org/10.1109/JSEN.2025.3543243.

19. M. Madagalam, M. Rosito, N. Blangetti, et al., "Unveiling the Effect of Bi in $ZnFe_2O_4$ Nanoparticles in Electrochemical Sensors," *Applied Surface Science* 673 (2024): 1–10.

20. G. Rodia, M. Bartoli, M. Etzi, S. Carrara, and A. Tagliaferro, "Ultrasound Assisted Poly(ethylene glycol) Templated Bismuth Oxynitrates Modified Screen-Printed Electrodes for Dopamine Electrochemical Detection," *Discover Electrochemistry* 2 (2025): 1–15.

21. D. Molino, G. Ferraro, S. Lettieri, et al., "Enhanced CO_2 Detection Using Potentiometric Sensors Based on PIM-1/DBU Imidazolate Membranes," *Advanced Sustainable Systems* 8 (2024): 1–10.

22. W. Li, G. Xie, X. Huo, et al., "Piezoelectric Composites for Gas Sensing: Evolution of Sensing and Transduction Designs," *Journal of Materials Chemistry C* 13 (2025): 13582–13606.

23. W. Li, X. Li, X. Xiao, et al., "A Multimodal Sensory Textile Using Programmable Ferroelectric Nanocomposites," *Advanced Materials* 37 (2025): e07169, https://doi.org/10.1002/adma.202507169.

24. J. Li, G. Xie, L. Dai, M. Yang, and Y. Su, "Rapid and Highly Selective Dopamine Sensing With CuInSe2-Modified Nanocomposite," *Journal of Composites Science* (2025): 123, https://doi.org/10.3390/jcs9030123.

25. J. Dai, G. Xie, X. Huo, J. Li, S. Deng, and Y. S. Su, "Implantable and Biodegradable Smart Textiles for Continuous Limb and Gastrointestinal Motility Monitoring," *Small* 21 (2025): 2407773.

26. S. A. Ahmed, T. Agnihotri, A. Ranjan, et al., "Boosting Stability in Ni-rich Cathodes: A Synergistic Approach to Surface and Bulk Modifications for Advanced Lithium-ion Batteries," *Journal of Materials Chemistry A* 13 (2025): 14846–14857, https://doi.org/10.1039/D4TA08834D.

27. C. Chen, C. Ren, S. Yang, et al., "Voice-driven Self-powered Ethanol Sensor for Speech Recognition and Drunk Driving Detection," *Sensors and Actuators B: Chemical* 447 (2025): 138869.

28. M. Madagalam, M. Bartoli, and A. M. Tagliaferro, "A Short Overview on Graphene and Graphene-Related Materials for Electrochemical Gas Sensing," *Materials* 17 (2024): 1–18.

29. Z. Shahrbabaki, S. Farajikhah, M. B. Ghasemian, et al., "A Flexible and Polymer-Based Chemiresistive CO_2 Gas Sensor at Room Temperature," *Advanced Materials Technologies* 8 (2023): 2201510, https://doi.org/10.1002/admt.202201510.

30. M. Wusiman and F. Taghipour, "Methods and Mechanisms of Gas Sensor Selectivity," *Critical Reviews in Solid State and Materials Sciences* 47 (2022): 416–435, https://doi.org/10.1080/10408436.2021.1941752.

31. C. Zhang, K. Xu, K. Liu, and J. Xu, "Metal Oxide Resistive Sensors for Carbon Dioxide Detection," *Coordination Chemistry Reviews* 472 (2022): 214758, https://doi.org/10.1016/j.ccr.2022.214758.

32. G. N. Korotcenkov, "Current Trends in Nanomaterials for Metal Oxide-Based Conductometric Gas Sensors: Advantages and Limitations. Part 1: 1D and 2D Nanostructures," *Nanomaterials* 10 (2020): 1–62.

33. G. N. Korotcenkov, "Electrospun Metal Oxide Nanofibers and Their Conductometric Gas Sensor Application. Part 2: Gas Sensors and Their Advantages and Limitations," *Nanomaterials* 11 (2021): 1–38.

34. G. Korotcenkov and V. P. N. Tolstoy, "Current Trends in Nanomaterials for Metal Oxide-Based Conductometric Gas Sensors: Advantages and Limitations—Part 2: Porous 2D Nanomaterials," *Nanomaterials* 13 (2023): 1–38.

35. E. Comini, "Integration of Metal Oxide Nanowires in Flexible Gas Sensing Devices," *Sensors* 13 (2013): 10659–10673, https://doi.org/10.3390/s130810659.

36. M. G. Mohamed, N. Y. Liu, A. F. EL-Mahdy, and S. W. Kuo, "Ultra-stable Luminescent Hybrid Microporous Polymers Based on Polyhedral Oligomeric Silsesquioxane for CO2 Uptake and Metal Ion Sensing," *Microporous and Mesoporous Materials* 311 (2021): 110695, https://doi.org/10.1016/j.micromeso.2020.110695.

37. F. Topuz, M. H. Abdellah, P. M. Budd, and M. A. Abdulhamid, "Advances in Polymers of Intrinsic Microporosity (PIMs)-Based Materials for Membrane, Environmental, Catalysis, Sensing and Energy Applications," *Polymer Reviews* 64 (2024): 251–305, https://doi.org/10.1080/15583724.2023.2236677.

38. P. M. Budd, N. B. McKeown, B. S. Ghanem, et al., "Gas Permeation Parameters and Other Physicochemical Properties of a Polymer of Intrinsic Microporosity: Polybenzodioxane PIM-1," *Journal of Membrane Science* 325 (2008): 851–860, https://doi.org/10.1016/j.memsci.2008.09.010.

39. N. Du, G. P. Robertson, J. Song, I. Pinnau, and M. D. M. Guiver, "High-Performance Carboxylated Polymers of Intrinsic Microporosity (PIMs) With Tunable Gas Transport Properties," *Macromolecules* 42 (2009): 6038–6043.

40. G. Cheng, B. Bonillo, R. S. Sprick, D. J. Adams, T. Hasell, and A. I. Cooper, "Conjugated Polymers of Intrinsic Microporosity (C-PIMs)," *Advanced Functional Materials* 24 (2014): 5219–5224, https://doi.org/10.1002/adfm.201401001.

41. D. M. Goodwin, M. Carta, M. M. Ali, D. Gillard, and O. Guy, "Enhanced Nitrogen Dioxide Detection Using Resistive Graphene-Based Electronic Sensors Modified With Polymers of Intrinsic Microporosity," *ACS Sensors* 10 (2025): 1378–1386, https://doi.org/10.1021/acssensors.4c03291.

42. W. Zhou, C. Yu, and X. Wang, "Fast and Quantitative Electrical Detection of Iodine Based on a Polymer of Intrinsic Microporosity," *ACS Applied Polymer Materials* 4 (2022): 9151–9159, https://doi.org/10.1021/acsapm.2c01479.

43. G. Ferraro, C. Astorino, M. Bartoli, et al., "Ionic Liquids–Polymer of Intrinsic Microporosity (PIMs) Blend Membranes for CO_2 Separation," *Membranes* 12 (2022): 1–13.

44. P. M. Budd, E. S. Elabas, B. S. Ghanem, et al., "Solution-Processed, Organophilic Membrane Derived from a Polymer of Intrinsic Microporosity," *Advanced Materials* 16 (2004): 456–459, https://doi.org/10.1002/adma.200306053.

45. H. Zhang, Y. Chen, A. Chu, H. Hu, and Y. Zhao, "Synthesis of Imidazole-Based Deep Eutectic Solvents as Solid Lubricants: Lubricated State Transition," *Materials* 16 (2023): 6579, https://doi.org/10.3390/ma16196579.

46. N. A. Husin, M. Muhamad, N. Yahaya, et al., "Application of a New Choline-imidazole Based Deep Eutectic Solvents in Hybrid Magnetic Molecularly Imprinted Polymer for Efficient and Selective Removal of Naproxen from Aqueous Samples," *Materials Chemistry and Physics* 261 (2021): 124228, https://doi.org/10.1016/j.matchemphys.2021.124228.

47. D. Nečas and P. Klapetek, "Gwyddion: An Open-Source Software for SPM Data Analysis," *Central European Journal of Physics* 10 (2012): 181–188.

48. M. Hayyan, F. S. Mjalli, M. A. Hashim, I. M. AlNashef, and T. X. Mei, "Investigating the Electrochemical Windows of Ionic Liquids," *Journal of Industrial and Engineering Chemistry* 19 (2013): 106–112, https://doi.org/10.1016/j.jiec.2012.07.011.

49. M. Yu, A. B. Foster, M. Alshurafa, et al., "CO2 separation Using Thin Film Composite Membranes of Acid-hydrolyzed PIM-1," *Journal of Membrane Science* 679 (2023): 121697, https://doi.org/10.1016/j.memsci.2023.121697.

50. M. Tamaddondar, A. B. Foster, M. Carta, P. Gorgojo, N. B. McKeown, and P. M. Budd, "Mitigation of Physical Aging with Mixed Matrix Membranes Based on Cross-Linked PIM-1 Fillers and PIM-1," *ACS Applied Materials & Interfaces* 12 (2020): 46756–46766, https://doi.org/10.1021/acsami.0c13838.

51. C. R. Mason, L. Maynard-Atem, K. W. J. Heard, et al., "Enhancement of CO_2 Affinity in a Polymer of Intrinsic Microporosity by Amine Modification," *Macromolecules* 47 (2014): 1021–1029.

52. F. Y. Li, Y. Xiao, T. S. Chung, and S. M. Kawi, "High-Performance Thermally Self-Cross-Linked Polymer of Intrinsic Microporosity (PIM-1) Membranes for Energy Development," *Macromolecules* 45 (2012): 1427–1437.

53. A. Y. Alentiev, G. N. Bondarenko, Y. V. Kostina, et al., "PIM-1/MIL-101 Hybrid Composite Membrane Material: Transport Properties and Free Volume," *Petroleum Chemistry* 54 (2014): 477–481, https://doi.org/10.1134/S0965544114070020.

54. L. Hao, K. S. Liao, and T. S. Chung, "Photo-oxidative PIM-1 Based Mixed Matrix Membranes with Superior Gas Separation Performance," *Journal of Materials Chemistry A* 3 (2015): 17273–17281, https://doi.org/10.1039/C5TA03776J.

55. Y. Liu, J. Zhang, and X. Tan, "High Performance of PIM-1/ZIF-8 Composite Membranes for O_2/N_2 Separation," *ACS Omega* 4 (2019): 16572–16577.

56. Q. Yang, W. Li, C. Dong, et al., "PIM-1 as an Artificial Solid Electrolyte Interphase for Stable Lithium Metal Anode in High-Performance Batteries," *Journal of Energy Chemistry* 42 (2020): 83–90, https://doi.org/10.1016/j.jechem.2019.06.012.

57. G. I. Badea, F. Gatea, S. C. Litescu-Filipescu, et al., "Optimization of Green Ultrasound-Assisted Extraction of Carotenoids and Tocopherol

from Tomato Waste Using NADESs," *Molecules* 30 (2025): 591, https://doi.org/10.3390/molecules30030591.

58. M. I. Martín, I. García-Díaz, M. L. Rodríguez, M. C. Gutiérrez, F. del Monte, and F. A. López, "Synthesis and Properties of Hydrophilic and Hydrophobic Deep Eutectic Solvents via Heating-stirring and Ultrasound," *Molecules* 29 (2024): 3089.

59. A. R. Lara-Hernández, N. V. Gallardo-Rivas, U. Páramo-García, R. Mayen-Mondragon, and S. B. Brachetti-Sibaja, "Effect of Alkyl-Chain-Length on the Electrochemical Behavior and Diffusion Coefficient of Imidazole- and Pyridine-Based Surfactants in Aqueous Solutions," *International Journal of Electrochemical Science* 16 (2021): 21101, https://doi.org/10.20964/2021.10.49.

60. T. Rajkumar and G. Ranga Rao, "Synthesis and Characterization of Hybrid Molecular Material Prepared by Ionic Liquid and Silicotungstic Acid," *Materials Chemistry and Physics* 112 (2008): 853–857, https://doi.org/10.1016/j.matchemphys.2008.06.046.

61. M. C. de ND and J. L. Walter, "Infrared and Raman spectra of heterocyclic compounds—I the infrared studies and normal vibrations of imidazole," *Spectrochimica Acta Part A: Molecular Spectroscopy* 24, no. (3), (1968): 52–237.

62. V. Furer, "Carbamate-group Conformation and IR Band Intensities," *Journal of Applied Spectroscopy* 53 (1990): 860–863, https://doi.org/10.1007/BF00659400.

63. E. D. Bates, R. D. Mayton, I. Ntai, and J. H. Davis, "CO 2 Capture by a Task-Specific Ionic Liquid," *Journal of the American Chemical Society* 124 (2002): 926–927, https://doi.org/10.1021/ja017593d.

64. N. Delgado-Mellado, M. Larriba, P. Navarro, et al., "Thermal Stability of Choline Chloride Deep Eutectic Solvents by TGA/FTIR-ATR Analysis," *Journal of Molecular Liquids* 260 (2018): 37–43, https://doi.org/10.1016/j.molliq.2018.03.076.

65. C. Astorino, E. De Nardo, S. Lettieri, G. Ferraro, C. F. Pirri, and S. Bocchini, "Advancements in Gas Separation for Energy Applications: Exploring the Potential of Polymer Membranes with Intrinsic Microporosity (PIM)," *Membranes* 13 (2023): 903, https://doi.org/10.3390/membranes13120903.

66. H. Maka and T. P. Spychaj, "Epoxy Resin Crosslinked with Conventional and Deep Eutectic Ionic Liquids," *Polimery* 57 (2012): 456–462.

67. G. Latini, M. Signorile, V. Crocellà, S. Bocchini, C. Pirri, and S. Bordiga, "Unraveling the CO_2 Reaction Mechanism in Bio-based Amino-acid Ionic Liquids by Operando ATR-IR Spectroscopy," *Catalysis Today* 336 (2019): 148–160, https://doi.org/10.1016/j.cattod.2018.12.050.

68. J.-Q. Li, M.-X. Jing, C. Han, et al., "A 3D Heterogeneous $FeTiO_3$ /TiO_2@C fiber Membrane as a Self-standing Anode for Power Li-ion Battery," *Applied Physics A* 124 (2018): 332, https://doi.org/10.1007/s00339-018-1750-y.

69. S. H. Yun, S. H. Shin, J. Y. Lee, et al., "Effect of Pressure on through-Plane Proton Conductivity of Polymer Electrolyte Membranes," *Journal of Membrane Science* 417–418 (2012): 210–216, https://doi.org/10.1016/j.memsci.2012.06.041.

70. J. Villalobos, R. Golnak, L. Xi, G. Schuck, and M. Risch, "Reversible and Irreversible Processes During Cyclic Voltammetry of an Electrodeposited Manganese Oxide as Catalyst for the Oxygen Evolution Reaction," *Journal of Physics: Energy* 2 (2020): 034009.

71. L. J. Nunes, "The rising threat of atmospheric CO2: a review on the causes, impacts, and mitigation strategies," *Environments* 10, no. (4) (2023): 66.

72. K. Permentier, S. Vercammen, S. Soetaert, and C. Schellemans, "Carbon Dioxide Poisoning: A Literature Review of an Often Forgotten Cause of Intoxication in the Emergency Department," *International Journal of Emergency Medicine* 10 (2017): 14, https://doi.org/10.1186/s12245-017-0142-y.

73. D. M. Makarov, M. A. Krestyaninov, A. A. Dyshin, V. A. Golubev, and A. M. Kolker, "CO_2 Capture Using Choline Chloride-based Eutectic Solvents. An Experimental and Theoretical Investigation," *Journal of Molecular Liquids* 413 (2024): 125910, https://doi.org/10.1016/j.molliq.2024.125910.

74. S. Dalbouha, M. Prakash, V. Timón, N. Komiha, M. Hochlaf, and M. L. Senent, "Explicitly Correlated Interaction Potential Energy Profile of Imidazole + CO_2 Complex," *Theoretical Chemistry Accounts* 134 (2015): 63, https://doi.org/10.1007/s00214-015-1657-z.

75. M. Han, S. Jung, Y. Lee, D. Jung, and S. H. Kong, "PEI-Functionalized Carbon Nanotube Thin Film Sensor for CO_2 Gas Detection at Room Temperature," *Micromachines* 12 (2021): 1053.

76. B. Andò, S. Baglio, D. Pasquale, et al., "Direct Printing of a Multi-Layer Sensor on Pet Substrate for CO_2 Detection," *Energies* 12 (2019): 557.

77. S. Srinives, T. Sarkar, R. Hernandez, and A. Mulchandani, "A Miniature Chemiresistor Sensor for Carbon Dioxide," *Analytica chimica acta* 874 (2015): 54–58, https://doi.org/10.1016/j.aca.2015.03.020.

78. S. Bag and K. Pal, "A PCB Based Chemiresistive Carbon Dioxide Sensor Operating at Room Temperature under Different Relative Humidity," *IEEE Transactions on Nanotechnology* 18 (2019): 1119–1128, https://doi.org/10.1109/TNANO.2019.2946837.

79. L. Liu, S. Sang, D. Han, et al., "PEI/PEG Functionalized Black Phosphorus Prepared by a One-Pot Method for a Wide Detection Range CO_2 Gas Sensor," *Sensors and Actuators B: Chemical* 369 (2022): 132303, https://doi.org/10.1016/j.snb.2022.132303.

80. S. Bag and K. Pal, "Sulfonated Poly (ether ether ketone) Based Carbon Dioxide Gas Sensor: Impact of Sulfonation Degree on Sensing Behavior at Different Humid Condition," *Sensors and Actuators B: Chemical* 303 (2020): 127115, https://doi.org/10.1016/j.snb.2019.127115.

Supporting Information

Additional supporting information can be found online in the Supporting Information section.

Supporting File: adsr70184-sup-0001-SuppMat.docx.